

Electron-only magnetic reconnection and inverse magnetic-energy transfer at sub-ion scales

Zhuo Liu,¹ Caio Silva,¹ Lucio M. Milanese,² Muni Zhou,³ Noah R. Mandell,⁴ and Nuno F. Loureiro¹

¹*Plasma Science and Fusion Center, Massachusetts Institute of Technology, Cambridge, MA 02139, USA*

²*Proxima Fusion GmbH, Munich, 81671, Germany*

³*School of Natural Sciences, Institute for Advanced Study, Princeton, NJ 08544, USA*

⁴*Princeton Plasma Physics Laboratory, Princeton, NJ 08543, USA*

(Dated: March 11, 2025)

We derive, and validate numerically, an analytical model for electron-only magnetic reconnection applicable to strongly magnetized plasmas. Our model predicts sub-ion-scale reconnection rates significantly higher than those pertaining to large-scale reconnection, aligning with recent observations and simulations. We apply this reconnection model to the problem of inverse magnetic energy transfer at sub-ion scales. We derive time-dependent scaling laws for the magnetic energy decay and the typical magnetic structure dimensions that differ from those previously found in the MHD regime. These scaling laws are validated via two- and three-dimensional simulations, demonstrating that sub-ion scale magnetic fields can reach large, system-size scales via successive coalescence.

Introduction. Decaying turbulence in plasmas is sometimes accompanied by the transfer of energy from small to large scales; a so-called inverse transfer. Though poorly understood, this phenomenon is thought to be crucial to magnetic field evolution at cosmological scales [1–3] as well as in various astrophysical systems such as the solar wind [4] and the heliosphere [5, 6]. The standard explanation for inverse energy transfer appeals to the conservation of net magnetic helicity [7–9]. However, recent studies have shown that this process can also occur in non-helical turbulent systems [10, 11]. It has been proposed that this may be due to the successive merger of magnetic structures via magnetic reconnection, thus transferring energy to progressively larger scales [12–17].

So far, investigations of this topic have mostly been restricted to the resistive MHD framework. This implies they cannot be directly applied to the (mostly) collisionless environments often encountered in astrophysical contexts. For example, recent *in-situ* spacecraft measurements have provided substantial evidence for the existence of numerous rope-like magnetic structures at ion scales, with substructures within these flux ropes observed at electron scales (e.g., [18–21]). As such, the existing understanding of inverse energy cascade needs to be extended to account for (i) kinetic modifications to turbulent dynamics; and (ii) changes to magnetic reconnection — as compared to resistive MHD systems.

The latter is of particular importance given the observation that the physics of reconnection between sub-ion-scale structures is expected to be substantially different: when the reconnection region is sufficiently small, the ions can become unresponsive, and a transition to so-called “electron-only reconnection” is expected. This variant of magnetic reconnection has been recently observed in the Earth’s magnetosphere [22, 23], and is numerically found to exhibit substantially higher reconnection rates compared to conventional scenarios [24–30].

The goal of this Letter is thus to generalize the current resistive-MHD-based understanding of inverse energy transfer via magnetic reconnection to kinetic, collisionless plasma environments.

Equations. We employ a two-field isothermal fluid model valid for low-beta plasmas [e.g., 31–35]. The dynamics of this system are described by equations for the perturbed electron density δn_e and the parallel (to the guide-field B_z) vector potential A_z , which read [36]:

$$\frac{1}{n_{0e}} \frac{d\delta n_e}{dt} = \hat{\mathbf{b}} \cdot \nabla \frac{e}{cm_e} d_e^2 \nabla_{\perp}^2 A_z, \quad (1)$$

$$\frac{d}{dt} (A_z - d_e^2 \nabla_{\perp}^2 A_z) = -c \frac{\partial \varphi}{\partial z} + \hat{\mathbf{b}} \cdot \nabla \frac{\delta n_e}{n_{0e}}. \quad (2)$$

Here, $\hat{\mathbf{b}} \cdot \nabla \equiv \partial/\partial z - 1/B_z \{A_z, \dots\}$ is the parallel (to the total field) gradient operator, and $d/dt \equiv \partial/\partial t + c/B_z \{\varphi, \dots\}$ denotes the convective time derivative, with φ the electrostatic potential; both operators feature a Poisson bracket, defined as $\{P, Q\} \equiv \partial_x P \partial_y Q - \partial_y P \partial_x Q$. These equations are closed via the gyrokinetic Poisson law [37],

$$\frac{\delta n_e}{n_{0e}} = \frac{T_{0e}}{T_{0i}} (\hat{\Gamma}_0 - 1) \frac{e\varphi}{T_{0e}}, \quad (3)$$

where $\hat{\Gamma}_0$ denotes the inverse Fourier transform of $\Gamma_0(\alpha) = I_0(\alpha)e^{-\alpha}$, with I_0 the zeroth-order modified Bessel function of the first kind and $\alpha = k_{\perp}^2 \rho_i^2/2$, where $\rho_i = v_{thi}/\Omega_i$ is the ion Larmor radius, with $v_{thi} = \sqrt{2T_{0i}/m_i}$ the ion thermal velocity and $\Omega_i = eB_z/m_i c$ the ion Larmor frequency. Lastly, $d_e = c/\omega_{pe}$ is the electron skin depth, with $\omega_{pe} = \sqrt{4\pi n_{0e} e^2/m_e}$ the electron plasma frequency. In the following, we refer to “perpendicular” as the direction perpendicular to the guide field B_z , i.e., the xy plane.

Electron-only Reconnection. We now use these equations to derive a two-dimensional reconnection model valid at scales below the ion Larmor radius. We consider

two identical magnetic islands with typical magnetic field B_\perp and radius R such that $d_e < R < \min(\rho_i, \rho_s)$ [38], merging in the x direction, where $\rho_s = \rho_i/\sqrt{2T_{0i}/T_{0e}}$ is the ion sound Larmor radius. The total magnetic flux to be reconnected is $A_{z,\text{total}} = B_\perp R$, and the time for this process to occur (reconnection time) is denoted as τ_{rec} . The width of the current sheet between the islands during reconnection is denoted as δ_x , assumed comparable to d_e (the scale at which the frozen flux condition is broken in our model, and the realizability is confirmed via direct numerical simulations below), and the length of the current sheet is denoted as δ_y . In the current sheet, $A_z = A_{z,\text{sheet}} \sim B_\perp \delta_x$, consistent with an upstream reconnecting field $B_y = \partial_x A_z \sim B_\perp$. The out-of-plane current in the sheet is then $-(4\pi/c)J_z = \nabla_\perp^2 A_z \sim B_\perp/\delta_x$.

In the sub-ion regime ($k_\perp \rho_i > 1$), ions are demagnetized, and Eq. (3) reduces to $\delta n_e/n_{0e} \approx -e\varphi/T_{0i}$; that is, electrons follow a Boltzmann response [32]. Thus, the advection of δn_e term in Eq. (1) vanishes. The advection of A_z term in Eq. (2), i.e., $\{\varphi, A_z\}$, becomes $-(cT_{0i}/eB_z)\{\delta n_e/n_{0e}, A_z\}$, which can be combined with the R.H.S. of Eq. (2). Taking $\partial_x \sim 1/\delta_x$ and $\partial_y \sim 1/\delta_y$ and balancing both sides of Eq. (1) within the sheet, we find $(\delta n_e/n_{0e})/\tau \sim (ed_e^2/B_z cm_e)(B_\perp^2/\delta_x \delta_y)$, where τ is the time it takes to reconnect the magnetic flux $A_{z,\text{sheet}}$. A similar term-balancing procedure for Eq. (2) yields $A_z/\tau \sim (c(T_{0e}+T_{0i})/eB_z n_{e0})(B_\perp \delta n_e/\delta_y)$. Note that the electron inertia term does not affect this balance since $d_e^2 \nabla_\perp^2 A_z \sim (d_e/\delta_x)^2 A_z \sim A_z$.

Combining these results, we find $\tau \sim (1/\sqrt{1+T_{0i}/T_{0e}})(\delta_y/\rho_s)(d_e/v_{A,\perp})$, where $v_{A,\perp} = B_\perp/\sqrt{4\pi n_0 m_i}$ is the (ion) Alfvén speed. The last step is to relate the reconnection time, τ_{rec} , and τ via $\tau_{\text{rec}}/\tau \sim A_{z,\text{total}}/A_{z,\text{sheet}} \sim R/d_e$. Writing the reconnection time in the form of $\tau_{\text{rec}} \sim \mathcal{R}_{\text{rec}}^{-1} R/v_{A,\perp}$, we obtain the normalized reconnection rate:

$$\mathcal{R}_{\text{rec}} \sim \sqrt{1 + \frac{T_{0i} \rho_s}{T_{0e} \delta_y}} \sim \sqrt{1 + \frac{T_{0i} \rho_s}{T_{0e} R}}, \quad (4)$$

where we have assumed $\delta_y \sim R$ (see Supplemental Material for validation). When $\rho_s > R$, the (normalized) reconnection rate can become much larger than the value of ~ 0.1 typically associated with collisionless reconnection [39–41] (but may not exceed $\sim \rho_s/d_e$). See Appendix A for further details.

The outflow velocity, u_{out} , can be estimated as the $E \times B$ drift velocity, i.e., $u_{\text{out}} \sim (c/B_x)E_z \sim cR/(d_e B_\perp)(B_\perp R/c\tau_{\text{rec}}) \sim \sqrt{1+T_{0i}/T_{0e}}(\rho_s/d_e)v_{A,\perp} \sim \sqrt{1+T_{0i}/T_{0e}}\sqrt{\beta_e}v_{Ae,\perp}$, with $v_{Ae,\perp} \equiv B_\perp/\sqrt{4\pi n_{0e} m_e}$ the electron Alfvén speed based on perpendicular magnetic field. The conclusion that the outflow velocity is proportional to electron Alfvén speed is consistent with previous laboratory observations [42]. Therefore, if instead we normalize the reconnection time to the outflow

time, i.e., $\tau_{\text{rec}} \sim \mathcal{R}_{\text{rec},e}^{-1} R/u_{\text{out}}$, we obtain

$$\mathcal{R}_{\text{rec},e} \sim d_e/R; \quad (5)$$

i.e., the aspect ratio of the reconnecting current sheet.

We now proceed to validate this model via direct numerical simulations. Eqs. (1,2,3) are solved numerically using the pseudo-spectral code GX [43, 44]. Hyperdiffusive terms of the form $\nu_H \nabla_\perp^6$ are added to the R.H.S. of Eqs. (1,2), with $\nu_H = 1/\Delta t(\Delta x/\pi)^6$; this value ensures that these terms are only significant at scales comparable to the grid scale. These terms are required to prevent the nonlinear unbounded thinning of the current sheet [45, 46]. These details apply to all the simulations we include in this Letter.

In what follows, all quantities are presented in dimensionless units. The simulations are performed in a doubly periodic box of dimensions $L_x \times L_y$, where $L_x = L_y = 2\pi$. The initial condition consists of two identical magnetic islands of Gaussian shape, specified as $A_z = A_0 \exp(-(2\pi a(x - 0.25L_x)/L_x)^2 - (2\pi a(y - 0.5L_y)/L_y)^2) + A_0 \exp(-(2\pi a(x - 0.75L_x)/L_x)^2 - (2\pi a(y - 0.5L_y)/L_y)^2)$ [47]. We set $a = 1.5$ so that the root-mean-squared width of each island is about 1.1, i.e., $R \approx 0.55$. Multiple simulations are performed by varying the values of ρ_i (we set $T_{i0}/T_{e0} = 1$ in all the simulations so $\rho_s = \rho_i/\sqrt{2}$) and d_e to encompass both the regime where $R > \rho_i > d_e$ (ion-coupled reconnection) and $\rho_i \gtrsim R > d_e$ (electron-only reconnection). All simulations have $\rho_i/d_e \leq 20$ so as to conform to the low-beta ordering that underlies the equations we use. The numerical resolution is adjusted across simulations to resolve the d_e scale adequately (see Supplemental Material for more information on simulation parameters).

For each simulation, we calculate the reconnection rate as the time derivative of the magnetic flux between the X- and the O-points. The peak reconnection rates are plotted in Fig. 1 against the parameter ρ_i/R . Along the horizontal axis, the progression from left to right signifies a transition from MHD to sub- ρ_i scales in terms of the initial island size. At MHD scales, we observe that the reconnection rate converges to a constant value ~ 0.2 , somewhat higher than the often quoted value of 0.1 [e.g., 39–41, 48–52] but consistent with previous results for collisionless reconnection in the strong guide-field limit [53, 54]. However, upon transition to sub-ion scales (i.e., $R \lesssim \rho_i$), the reconnection rates exhibit a substantial increase, aligning almost perfectly with our model's prediction, Eq. (4), represented by the dashed line in Fig. 1. Moreover, we notice that the agreement with Eq. (4) is already very good when $R \approx \rho_i$ and $R/d_e \lesssim 5$. Therefore, large scale separation between ρ_i and d_e does not appear to be necessary for Eq. (4) to be valid (see [38]). Consistently, at fixed ρ_i/R , the reconnection rate depends only weakly on the value of d_e (and this dependence weakens as d_e becomes smaller); while

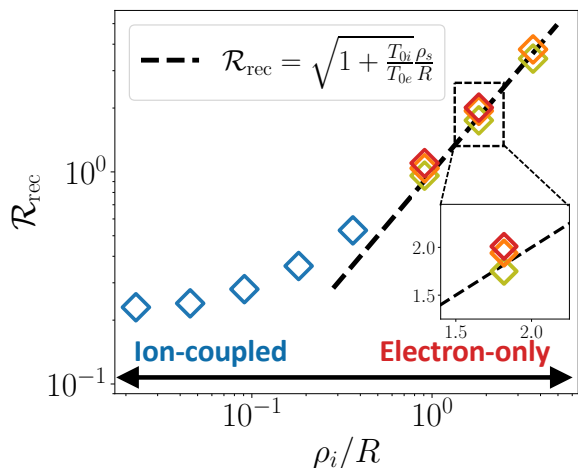


FIG. 1: Dimensionless peak reconnection rates, \mathcal{R}_{rec} , from simulations with different values of ρ_i/R . In the electron-only regime ($\rho_i \gtrsim R > d_e$), red, orange, and yellow symbols refer to simulations with $d_e/R = 0.09, 0.18, 0.36$, respectively. In the ion-coupled regime ($R > \rho_i > d_e$), we set $d_e/\rho_i = 0.1$ (except for the leftmost data-point, where $d_e/\rho_i = 0.2$). The dashed line is Eq. (4) (with $T_{i0}/T_{e0} = 1$).

we confirm that $\delta_x \sim d_e$ approximately holds for each simulation.

We also note that the reconnection rate starts to significantly deviate from the large-scale (ion-coupled) value (~ 0.2) at around $R \sim 10\rho_i$. This observation is consistent with the analysis in [55] and with simulation results [25], where it is predicted that ions start to decouple from the reconnecting magnetic field at scales of around 10 ion-scales. However, it is not until $R \sim \rho_i$ that the reconnection rate perfectly aligns with Eq. (4).

Lastly, we note that it is possible to extend our analytical model to the $\beta \sim 1$ case — see Supplemental Material, Section 2. In that regime, we again find that the reconnection rate is proportional to $1/R$.

Magnetic Flux Tube Coalescence. We now apply the electron-only reconnection model to the problem of inverse transfer of magnetic energy at sub-ion scales within the framework of Eqs. (1-3). We first address two-dimensional dynamics in the perpendicular plane. Consider two identical circular magnetic islands of radius R such that $\rho_i \gtrsim R > d_e$. Each carries the magnetic flux RB_{\perp} , which is assumed to be conserved by their merger [12, 13]. The lifetime of these two islands is determined by the reconnection time, $\tau_{\text{rec}} \sim (R/\rho_s)(R/v_{A,\perp})$, as shown above. Using the conservation of magnetic flux (and noting that $v_{A,\perp} \propto B_{\perp}$ and ρ_s is independent of B_{\perp} under the strong guide field condition), we find $R \propto B_{\perp}^{-1}$ and, thus, $\tau_{\text{rec}} \propto B_{\perp}^{-3}$.

Now considering a “sea” of (volume-filling) magnetic islands with similar sizes in the sub- ρ_i regime and assum-

ing the merging process to occur sequentially between island pairs, the evolution of total magnetic energy can be described by

$$\frac{d\mathcal{E}}{dt} \propto \frac{dB_{\perp}^2}{dt} \sim -\frac{B_{\perp}^2}{\tau_{\text{rec}}} \propto -B_{\perp}^5 \propto \mathcal{E}^{5/2}. \quad (6)$$

We thus find $\mathcal{E} = [a(t - t_0) + \mathcal{E}_0^{-3/2}]^{-2/3}$, where t_0 is the lifetime of the first island generation, a is a coefficient, and \mathcal{E}_0 is the initial magnetic energy. The perpendicular coherence scale and magnetic field strength can be derived in a similar way. The resulting long-term ($\tilde{t} \equiv t/t_0 \gg 1$) evolution scaling laws are

$$k_{\perp} \propto \tilde{t}^{-1/3}, \quad B_{\perp} \propto \tilde{t}^{-1/3}, \quad \mathcal{E} \propto \tilde{t}^{-2/3}. \quad (7)$$

When extending to the three-dimensional case (with a strong guide field), a magnetic island of radius R and magnetic field B_{\perp} becomes a magnetic flux tube with radius R , poloidal magnetic field B_{\perp} , and length l in the direction of the local mean field. The arguments above leading to Eq. (7) should remain valid (which we will confirm via direct numerical simulation). The length of the flux tube l can be estimated from the assumption that the inverse linear time scale, $\gamma_l \sim \omega_{KAW} \sim k_{\perp}\rho_s k_{\parallel} v_A$ (with $k_{\perp} \sim 1/R$ and $l \sim 1/k_{\parallel}$), should be comparable to the inverse nonlinear time scale, γ_{nl}^{-1} (critical balance [56]), where γ_{nl}^{-1} should be the smallest of the reconnection time, τ_{rec} , and the perpendicular advection time, R/u_{\perp} , with $u_{\perp} \sim (c/B_z)\varphi/R$ being the in-plane ($\mathbf{E} \times \mathbf{B}$) velocity that pertains to Eqs. (1-2). By assuming scale-by-scale equipartition between the density and magnetic energy fluctuations, $(\delta n_e/n_{0e})^2 n_{0e} T_{0e} \sim |\nabla_{\perp} A_z|^2/8\pi$ [35] (see Section 5 of the Supplemental Material for validation of this hypothesis), together with Eq. (3) in the limit $k_{\perp}\rho_i > 1$, we find $\varphi \sim \sqrt{T_{0i}/T_{0e}}(\rho_i v_A/c)B_{\perp}$ and, thus, $R/u_{\perp} \sim (R/\rho_s)(R/v_{A,\perp}) \sim \tau_{\text{rec}}$. Therefore, we conclude that the nonlinear advection time and reconnection time are comparable within this regime, i.e., $\gamma_{nl} \sim \tau_{\text{rec}}^{-1} \sim k_{\perp}\rho_s k_{\parallel} v_{A,\perp}$. This conclusion differs from that in the MHD regime, where reconnection is always slower [13]. Finally, balancing γ_l with γ_{nl} yields

$$l \sim B_z/(k_{\perp}B_{\perp}) \propto \tilde{t}^{2/3}. \quad (8)$$

To verify these predictions, we conducted a three-dimensional simulation in a periodic domain with dimensions $L_x \times L_y \times L_z$, where $L_x = L_y = 2\pi$ and $L_z = 4L_x$ (in normalized units). We specify the initial equilibrium as $A_z(x, y, z, t = 0) = A_{z0} \cos(k_0 x) \cos(k_0 y)$ with $k_0 = 10$ and $A_{z0} = 0.1$, yielding a $2k_0 \times 2k_0$ static array of magnetic flux tubes with sequentially opposite polarities. We set $\rho_i = 1.0$ (and $T_{i0} = T_{e0}$) and $d_e = 0.04$. These choices ensure that all flux tubes satisfy $d_e < R < \rho_i$, and thus Eqs. (7-8) should be valid after an initial transient. We note that because all initial magnetic structures are small-scale, magnetic energy can only reach larger scales

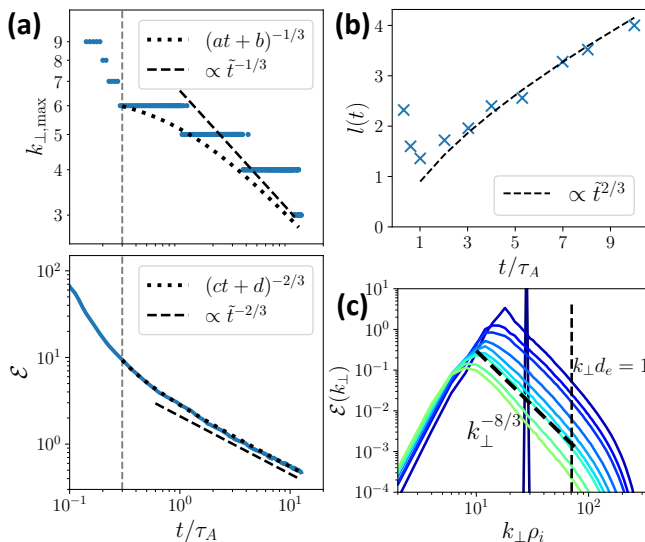


FIG. 2: Three-dimensional simulation results. (a) Temporal evolution of the wavenumber corresponding to the peak of the magnetic spectrum (top panel) and total magnetic energy (bottom panel). a, b, c, d are fitting parameters. We use the data to the right of the gray vertical dashed lines to avoid the transient stage. (b) Parallel coherence length l at different times. (c) The perpendicular magnetic spectra at progressively later times (from blue to green). The vertical dashed line denotes the d_e scale.

through inverse transfer, that is, magnetic island mergers.

Fig. 2 presents the temporal evolution of some key quantities. The top panel of Fig. 2 (a) shows the time evolution of the wavenumber at which the magnetic energy spectrum peaks, $k_{\perp, \max}$; whereas the bottom panel shows the box-averaged magnetic energy, \mathcal{E} . Both quantities conform to the theoretical predictions after $t \approx 0.3\tau_A$, with the scaling laws of Eq. (7) becoming applicable for $t \gtrsim 1.0\tau_A$ [57]. Likewise, the parallel coherence length l , estimated using the five-point second-order structure function [35, 58, 59] (see the Supplemental Material for further details), aligns with Eq. (8) after approximately $t \approx 2.0\tau_A$, as evident from Fig. 2 (b) [60]. We find (see Supplemental Material) that these temporal power laws also hold in the non-isothermal limit.

Fig. 2 (c) shows the evolution of the perpendicular magnetic-energy spectrum. A reasonable agreement with a $k_{\perp}^{-8/3}$ [35, 61] inertial-range power-law behavior is observed, suggesting that, in addition to the inverse cascade arising from the flux-tube merger (which accounts for the shift of the peak of the magnetic spectrum to smaller values of k_{\perp}), there is also a direct cascade driven by the nonlinear interaction of kinetic Alfvén wave packets maintaining the $-8/3$ spectrum (see Section 3 of the

Supplemental Material for energy transfer diagnostics). This observation is consistent with measurements of turbulence in the Earth’s magnetosheath in instances where electron-only reconnection is prevalent [23].

The similarity between the reconnection and the eddy turn-over times implies that, in our simulations, the inverse and forward energy cascades should indeed be comparable (see Section 3 of the Supplemental Material for evidence). However, we note that in systems where magnetic islands are not as volume-filling as in our numerical setup, the inverse cascade would not be expected to be energetically significant, and the forward cascade should dominate.

Transition to MHD scales. As the flux tube (or island) merging proceeds, structures get progressively larger and eventually transition to MHD scales, i.e., $R \gg \rho_i$. In this regime, electron-only reconnection no longer applies; instead, we expect the (normalized) reconnection rate to be a constant, independent of either the island size or the kinetic scales (Fig. 1 indicates $\mathcal{R}_{\text{rec}} \approx 0.2$). This observation, together with flux conservation, is all that is required to conclude that, at this stage, the evolution scalings of resistive MHD [12, 13, 15] should apply here as well. Namely, we expect

$$k_{\perp} \propto \tilde{t}^{-1/2}, \quad B \propto \tilde{t}^{-1/2}, \quad \mathcal{E} \propto \tilde{t}^{-1}. \quad (9)$$

To directly investigate these predictions, we conducted a two-dimensional simulation for which the initial condition is $\hat{A}_z(\mathbf{k}_{\perp}) = A_{z0}(k_{\perp}^4/k_c^4) \exp(i\phi(\mathbf{k}_{\perp}))$ for $k_{\perp} \leq k_c$ and $\hat{A}_z(\mathbf{k}_{\perp}) = A_{z0}(k_{\perp}^4/k_c^4) \exp(1 - k_{\perp}^4/k_c^4) \exp(i\phi(\mathbf{k}_{\perp}))$ for $k_{\perp} > k_c$, where $\phi(\mathbf{k}_{\perp})$ is a random phase, $A_{z0} = 0.001$ and $k_c = 160$. The initial magnetic spectrum is still a very narrow spike at very small scales (see the dark blue spike in Fig. 2 (c)). The domain is a doubly periodic box of dimensions $L_x \times L_y$, with $L_x = L_y = 2\pi$, and the spatial grid size is 8192^2 . We set $\rho_i = 0.025$ ($\rho_s \approx 0.0177$) and $d_e = 0.002$, so that the initial condition satisfies $\rho_i^{-1} < k_c < d_e^{-1}$; thus, this simulation should first capture merging at kinetic scales (as in the 3D simulation discussed earlier), followed by a transition to MHD scales.

Time traces of magnetic energy \mathcal{E} and characteristic radius R of the magnetic structures, defined as $R \equiv 2\pi/4k_{\perp, \max}$, are presented in Fig. 3. Initially, these quantities are found to evolve according to the power laws $\tilde{t}^{-2/3}$ and $\tilde{t}^{1/3}$, respectively, in accordance with Eq. (7). As R exceeds ρ_i (around $t \approx 0.1\tau_A$) the evolution of these quantities starts to deviate from those power laws. This threshold is consistent with the departure from the electron-only reconnection regime (i.e., Eq. (4)) as ρ_i/R decreases identified in Fig. 1. Around $t \approx 10.0\tau_A$, R reaches $10\rho_i$, the scale at which the reconnection rate converges to the constant large-scale value and ions are fully coupled (see Fig. 1). Consistently, transitions to $\mathcal{E} \sim \tilde{t}^{-1}$ and $R \sim \tilde{t}^{1/2}$ power-law scalings are observed, in agreement with the predictions of Eq. (9).

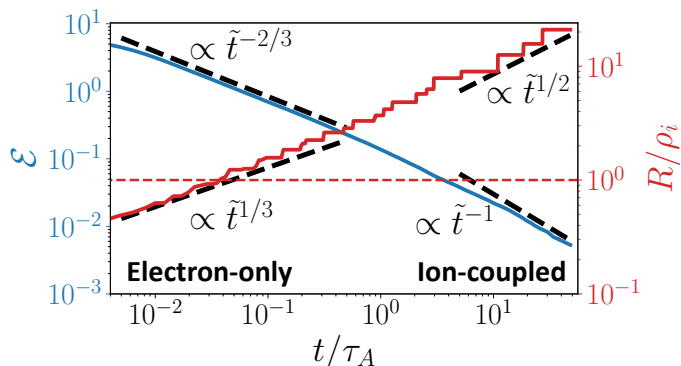


FIG. 3: Temporal evolution of magnetic energy \mathcal{E} (blue) and characteristic island radius R (red) from the two-dimensional simulation. The horizontal red dashed line denotes $R = \rho_i$.

Conclusions. We present an analytical model for electron-only strong-guide-field reconnection in low- β plasmas. Unlike large-scale collisionless reconnection, where the (normalized) reconnection rate is conjectured to be a constant of order 0.1 [40, 41], we find that this regime is characterized by reconnection rates that scale as the ratio between the ion gyroradius and the size of the reconnecting structure and which can significantly exceed 0.1. This finding provides a theoretical explanation for previous observational and numerical studies [e.g., 25, 29, 30]. The validity of our model is confirmed through direct numerical simulations, which also reveal that deviation from the fully ion-coupled regime begins when $R \approx 10\rho_i$, consistent with previous numerical studies [25] in a different plasma regime. Although our focus in this study is low beta plasmas, we also propose an extension of our derivation to $\beta_e \sim 1$ (see Supplemental Material) which appears to be consistent with existing numerical data.

Using this reconnection model, we derive time-dependent scaling laws for inverse magnetic-energy transfer in the sub- ρ_i range, which we validate via a three-dimensional direct numerical simulation. Finally, through a two-dimensional simulation starting with random Gaussian magnetic fields, we demonstrate the ability of magnetic-island mergers to transport magnetic energy from kinetic to MHD scales, accompanied by predicted changes in the time-dependent scaling laws. In addition to its relevance to the understanding of the self-organization of systems dominated by flux-rope-like structures [e.g., 20, 62, 63], this conclusion lends credence to recently proposed ideas for the viability of electron-scale seeds as the origin of large-scale magnetic fields [13, 64, 65].

Acknowledgements. This work was supported by DOE Awards DE-SC0022012, DE-FG02-91-ER54109, and by the Schmidt Futures at the Institute for Advanced Study. This work used resources of the Satori

cluster at the MGHPCC facility funded by DOE award No. DE-FG02-91-ER54109, and the National Energy Research Scientific Computing Center, a DOE Office of Science User Facility supported by the Office of Science of the U.S. Department of Energy under Contract No. DE-AC02-05CH11231 using NERSC award FES-ERCAP0020063.

Appendix A: Further details of reconnection rate derivation

A schematic of the reconnection configuration under consideration is shown in Fig. 4. The key quantities associated with the magnetic islands are the radius R , the reconnecting magnetic field B_\perp , and the total magnetic flux $A_{z,\text{total}} = B_\perp R$. For the current sheet, the relevant quantities are its width $\delta_x \sim d_e$, its length $\delta_y \sim R$, the reconnecting flux $A_{z,\text{sheet}} = B_\perp \delta_x$, and the out-of-plane current $\nabla_\perp^2 A_{z,\text{sheet}} = -(4\pi/c)J_z \sim B_\perp/\delta_x$ (derived from Ampere's law).

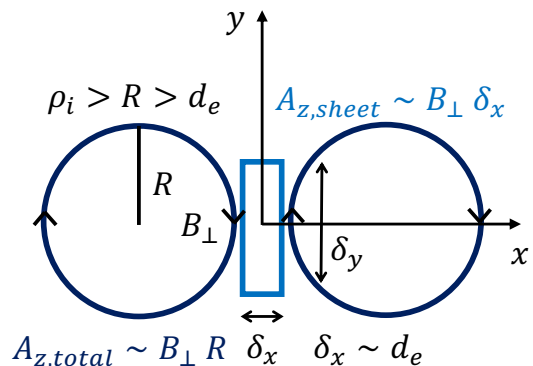


FIG. 4: A schematic of electron-only reconnection configuration. Two magnetic islands (represented by dark blue circles) of radius R such that $d_e < R < \rho_i$ and magnetic field B_\perp reconnect with each other via a current sheet (central blue rectangle) of dimensions $\delta_x \sim d_e$ and $\delta_y \sim R$.

We start by rewriting Eqs. (1-3) in their 2D form:

$$\frac{\partial \delta n_e / n_{0e}}{\partial t} + \frac{c}{B_0} \{ \varphi, \delta n_e / n_{0e} \} = \frac{1}{B_0} \left\{ A_\parallel, \frac{e}{cm_e} d_e^2 \nabla_\perp^2 A_\parallel \right\}, \quad (\text{A1})$$

$$\begin{aligned} & \frac{\partial (A_\parallel - d_e^2 \nabla_\perp^2 A_\parallel)}{\partial t} + \frac{c}{B_0} \{ \varphi, A_\parallel - d_e^2 \nabla_\perp^2 A_\parallel \} \\ & = - \frac{c T_{0e}}{e} \frac{1}{B_0} \left\{ A_\parallel, \frac{\delta n_e}{n_{0e}} \right\} \end{aligned} \quad (\text{A2})$$

$$\frac{\delta n_e}{n_{0e}} = \frac{T_{0e}}{T_{0i}} (\hat{\Gamma}_0 - 1) \frac{e\varphi}{T_{0e}}. \quad (\text{A3})$$

In the large $k_{\perp}\rho_i$ limit, Eq. (A3) reduces to [32]

$$\frac{\delta n_e}{n_{0e}} = -\frac{e\varphi}{T_{0i}}. \quad (\text{A4})$$

Next, we balance the terms in the above equations within the current sheet, where the spatial derivatives are approximated as $\partial_x \sim 1/\delta_x \sim 1/d_e$ and $\partial_y \sim 1/\delta_y \sim 1/R$. We introduce τ , the time taken to reconnect the flux within the current sheet, represented by $A_{z,\text{sheet}}$.

In Eq. (A1), the Poisson bracket between φ and δn_e vanishes due to Eq. (A4). The remaining terms are estimated as:

$$\begin{aligned} \frac{\delta n_e/n_{0e}}{\tau} &\sim \frac{ed_e^2}{B_0cm_e} \partial_x A_{z,\text{sheet}} \partial_y \nabla_{\perp}^2 A_{z,\text{sheet}} \\ &\sim \frac{ed_e^2}{B_0cm_e} B_{\perp} \frac{B_{\perp}/\delta_x}{R}. \end{aligned} \quad (\text{A5})$$

In Eq. (A2), since $d_e^2 \nabla_{\perp}^2 A_{z,\text{sheet}} \sim d_e^2 B_{\perp}/\delta_x \sim (d_e/\delta_x)^2 A_{z,\text{sheet}} \sim A_{z,\text{sheet}}$, the electron inertial term $d_e^2 \nabla_{\perp}^2 A_{z,\text{sheet}}$ does not affect term balancing. The other terms are estimated as

$$\begin{aligned} \frac{A_{z,\text{sheet}}}{\tau} &\sim \frac{c(T_{0e} + T_{0i})}{eB_0} \partial_x A_{z,\text{sheet}} \partial_y (\delta n_e/n_{0e}) \\ &\sim \frac{c(T_{0e} + T_{0i})}{eB_0} B_{\perp} \frac{\delta n_e/n_{0e}}{R}, \end{aligned} \quad (\text{A6})$$

noting that the two Poisson brackets combine using Eq. (A4).

Combining Eq. (A5) and Eq. (A6) to eliminate $\delta n_e/n_{0e}$, we derive

$$\tau \sim \frac{1}{\sqrt{1 + T_{0i}/T_{0e}}} \frac{R}{\rho_s} \frac{d_e}{v_{A,\perp}}, \quad (\text{A7})$$

where $v_{A,\perp} = B_{\perp}/\sqrt{4\pi n_0 m_i}$.

Finally, the reconnection time τ_{rec} , representing the time taken to reconnect the entire magnetic flux, relates to τ via $\tau_{\text{rec}}/\tau \sim A_{z,\text{total}}/A_{z,\text{sheet}}$. Thus, we obtain:

$$\tau_{\text{rec}} \sim \frac{1}{\sqrt{1 + T_{0i}/T_{0e}}} \frac{R}{\rho_s} \frac{R}{v_{A,\perp}}. \quad (\text{A8})$$

[1] R. Banerjee and K. Jedamzik, Evolution of cosmic magnetic fields: From the very early universe, to recombination, to the present, *Phys. Rev. D* **70**, 123003 (2004).
 [2] R. Durrer and A. Neronov, Cosmological magnetic fields: their generation, evolution and observation, *The Astronomy and Astrophysics Review* **21**, 1 (2013).
 [3] D. N. Hosking and A. A. Schekochihin, Cosmic-void observations reconciled with primordial magnetogenesis, *Nature Communications* **14**, 7523 (2023).
 [4] C. Chen, A. Mallet, T. Yousef, A. Schekochihin, and T. Horbury, Anisotropy of Alfvénic turbulence in the solar wind and numerical simulations, *Monthly Notices of the Royal Astronomical Society* **415**, 3219 (2011).

[5] O. Khabarova, G. Zank, G. Li, J. Le Roux, G. Webb, A. Dosch, and O. Malandraki, Small-scale magnetic islands in the solar wind and their role in particle acceleration. i. dynamics of magnetic islands near the heliospheric current sheet, *The Astrophysical Journal* **808**, 181 (2015).
 [6] J. Drake, M. Swisdak, and R. Fermo, The power-law spectra of energetic particles during multi-island magnetic reconnection, *The Astrophysical Journal Letters* **763**, L5 (2012).
 [7] A. Pouquet, On two-dimensional magnetohydrodynamic turbulence, *Journal of Fluid Mechanics* **88**, 1 (1978).
 [8] W. Matthaeus and S. L. Lamkin, Turbulent magnetic reconnection, *The Physics of fluids* **29**, 2513 (1986).
 [9] M. Christensson, M. Hindmarsh, and A. Brandenburg, Inverse cascade in decaying three-dimensional magnetohydrodynamic turbulence, *Physical Review E* **64**, 056405 (2001).
 [10] A. Brandenburg, T. Kahniashvili, and A. G. Tevzadze, Nonhelical inverse transfer of a decaying turbulent magnetic field, *Physical review letters* **114**, 075001 (2015).
 [11] J. Reppin and R. Banerjee, Nonhelical turbulence and the inverse transfer of energy: A parameter study, *Physical Review E* **96**, 053105 (2017).
 [12] M. Zhou, P. Bhat, N. F. Loureiro, and D. A. Uzdensky, Magnetic island merger as a mechanism for inverse magnetic energy transfer, *Physical Review Research* **1**, 012004 (2019).
 [13] M. Zhou, N. F. Loureiro, and D. A. Uzdensky, Multi-scale dynamics of magnetic flux tubes and inverse magnetic energy transfer, *Journal of Plasma Physics* **86**, 535860401 (2020).
 [14] P. Bhat, M. Zhou, and N. F. Loureiro, Inverse energy transfer in decaying, three-dimensional, non-helical magnetic turbulence due to magnetic reconnection, *Monthly Notices of the Royal Astronomical Society* **501**, 3074 (2021).
 [15] M. Zhou, D. H. Wu, N. F. Loureiro, and D. A. Uzdensky, Statistical description of coalescing magnetic islands via magnetic reconnection, *Journal of Plasma Physics* **87**, 905870620 (2021).
 [16] D. N. Hosking and A. A. Schekochihin, Reconnection-controlled decay of magnetohydrodynamic turbulence and the role of invariants, *Physical Review X* **11**, 041005 (2021).
 [17] L. M. Milanese, *Turbulent Dynamics Under Two Ideal Invariants: Dynamic Phase Alignment in Plasmas and Nonionized Fluids*, Phd thesis, Massachusetts Institute of Technology, Cambridge, MA (2023), available at <https://hdl.handle.net/1721.1/151221>.
 [18] J. Stawarz, J. Eastwood, K. Genestreti, R. Nakamura, R. Ergun, D. Burgess, J. Burch, S. Fuselier, D. Gershman, B. L. Giles, *et al.*, Intense electric fields and electron-scale substructure within magnetotail flux ropes as revealed by the magnetospheric multiscale mission, *Geophysical Research Letters* **45**, 8783 (2018).
 [19] Z. Zhong, M. Zhou, R. Tang, X. Deng, D. Turner, I. Cohen, Y. Pang, H. Man, C. Russell, B. Giles, *et al.*, Direct evidence for electron acceleration within ion-scale flux rope, *Geophysical Research Letters* **47**, e2019GL085141 (2020).
 [20] S. Huang, Q. Xiong, L. Song, J. Nan, Z. Yuan, K. Jiang, X. Deng, and L. Yu, Electron-only reconnection in an ion-scale current sheet at the magnetopause, *The Astro-*

- physical Journal **922**, 54 (2021).
- [21] H. Hasegawa, R. Denton, K. Dokgo, K.-J. Hwang, T. Nakamura, and J. Burch, Ion-scale magnetic flux rope generated from electron-scale magnetopause current sheet: Magnetospheric multiscale observations, *Journal of Geophysical Research: Space Physics* **128**, e2022JA031092 (2023).
- [22] T. Phan, J. P. Eastwood, M. Shay, J. Drake, B. Ö. Sonnerup, M. Fujimoto, P. Cassak, M. Øieroset, J. Burch, R. Torbert, *et al.*, Electron magnetic reconnection without ion coupling in earth's turbulent magnetosheath, *Nature* **557**, 202 (2018).
- [23] J. E. Stawarz, J. P. Eastwood, T. Phan, I. Gingell, M. Shay, J. Burch, R. Ergun, B. Giles, D. Gershman, O. Le Contel, *et al.*, Properties of the turbulence associated with electron-only magnetic reconnection in earth's magnetosheath, *The Astrophysical journal letters* **877**, L37 (2019).
- [24] N. Jain, A. S. Sharma, L. Zelenyi, and H. Malova, Electron scale structures of thin current sheets in magnetic reconnection, in *Annales geophysicae*, Vol. 30 (Copernicus Publications Göttingen, Germany, 2012) pp. 661–666.
- [25] P. Sharma Pyakurel, M. Shay, T. Phan, W. Matthaeus, J. Drake, J. TenBarge, C. Haggerty, K. Klein, P. Cassak, T. Parashar, *et al.*, Transition from ion-coupled to electron-only reconnection: Basic physics and implications for plasma turbulence, *Physics of Plasmas* **26** (2019).
- [26] F. Califano, S. S. Cerri, M. Faganello, D. Laveder, M. Sisti, and M. W. Kunz, Electron-only reconnection in plasma turbulence, *Frontiers in Physics* **8**, 317 (2020).
- [27] G. Arrò, F. Califano, and G. Lapenta, Statistical properties of turbulent fluctuations associated with electron-only magnetic reconnection, *Astronomy & Astrophysics* **642**, A45 (2020).
- [28] C. Vega, V. Roytershteyn, G. L. Delzanno, and S. Boldyrev, Electron-only reconnection in kinetic-Alfvén turbulence, *The Astrophysical Journal Letters* **893**, L10 (2020).
- [29] S. Greess, J. Egedal, A. Stanier, J. Olson, W. Daughton, A. Lê, A. Millet-Ayala, C. Kuchta, and C. Forest, Kinetic simulations verifying reconnection rates measured in the laboratory, spanning the ion-coupled to near electron-only regimes, *Physics of Plasmas* **29** (2022).
- [30] Y. Guan, Q. Lu, S. Lu, K. Huang, and R. Wang, Reconnection rate and transition from ion-coupled to electron-only reconnection, *The Astrophysical Journal* **958**, 172 (2023).
- [31] A. A. Schekochihin, S. C. Cowley, W. Dorland, G. W. Hammett, G. G. Howes, E. Quataert, and T. Tatsuno, Astrophysical gyrokinetics: kinetic and fluid turbulent cascades in magnetized weakly collisional plasmas, *The Astrophysical Journal Supplement Series* **182**, 310 (2009).
- [32] A. Zocco and A. A. Schekochihin, Reduced fluid-kinetic equations for low-frequency dynamics, magnetic reconnection, and electron heating in low-beta plasmas, *Physics of Plasmas* **18** (2011).
- [33] T. Passot, P. L. Sulem, and E. Tassi, Gyrofluid modeling and phenomenology of low- β_e Alfvén wave turbulence, *Physics of Plasmas* **25**, 042107 (2018).
- [34] R. Meyrand, J. Squire, A. A. Schekochihin, and W. Dorland, On the violation of the zeroth law of turbulence in space plasmas, *Journal of Plasma Physics* **87** (2021).
- [35] M. Zhou, Z. Liu, and N. F. Loureiro, Spectrum of kinetic-Alfvén-wave turbulence: intermittency or tearing mediation?, *Monthly Notices of the Royal Astronomical Society* **524**, 5468 (2023).
- [36] These equations are the isothermal limit of the Kinetic Reduced Electron Heating Model (KREHM), a rigorous analytical framework derived from gyrokinetics under the condition of low electron plasma beta ($\beta_e \sim m_e/m_i$, where β_e is the ratio of the electron to the magnetic pressure, and m_e and m_i are the electron and proton masses) [32]. See Supplemental Material for more details and results in the non-isothermal limit.
- [37] J. A. Krommes, Fundamental statistical descriptions of plasma turbulence in magnetic fields, *Physics Reports* **360**, 1 (2002).
- [38] We use $<$ instead of \ll in order not to interfere with the ordering under which Eqs. (1-3) are derived (namely, $\beta \sim m_e/m_i$ so that $\rho_i \sim d_e$, see [32]). We note that β does not have to be numerically close to m_e/m_i ; all that is formally required is for ρ_i/d_e not to be so large as to interfere with the asymptotic expansion parameters. Empirically, it is known that Eqs. (1-3) remain valid at least up to $\beta \sim 0.1$ (see [82]). In practice, a maximum ratio of $\rho_i/d_e \approx 20$ is acceptable if adopting the real proton-electron mass ratio.
- [39] J. Birn, J. F. Drake, M. A. Shay, B. N. Rogers, R. E. Denton, M. Hesse, M. Kuznetsova, Z. W. Ma, A. Bhattacharjee, A. Otto, and P. L. Pritchett, Geospace environmental modeling (gem) magnetic reconnection challenge, *Journal of Geophysical Research: Space Physics* **106**, 3715 (2001).
- [40] P. Cassak, Y.-H. Liu, and M. Shay, A review of the 0.1 reconnection rate problem, *Journal of Plasma Physics* **83**, 715830501 (2017).
- [41] Y.-H. Liu, M. Hesse, F. Guo, W. Daughton, H. Li, P. Cassak, and M. Shay, Why does steady-state magnetic reconnection have a maximum local rate of order 0.1?, *Physical Review Letters* **118**, 085101 (2017).
- [42] P. Shi, P. Srivastav, M. H. Barbhuiya, P. A. Cassak, E. E. Scime, and M. Swisdak, Laboratory observations of electron heating and non-maxwellian distributions at the kinetic scale during electron-only magnetic reconnection, *Physical Review Letters* **128**, 025002 (2022).
- [43] N. Mandell, W. Dorland, and M. Landreman, Laguerre-Hermite pseudo-spectral velocity formulation of gyrokinetics, *Journal of Plasma Physics* **84**, 905840108 (2018).
- [44] N. Mandell, W. Dorland, I. Abel, R. Gaur, P. Kim, M. Martin, and T. Qian, Gx: a gpu-native gyrokinetic turbulence code for tokamak and stellarator design, arXiv preprint arXiv:2209.06731 (2022).
- [45] B. Rogers and L. Zakharov, Collisionless $m=1$ reconnection in tokamaks, *Physics of Plasmas* **3**, 2411 (1996).
- [46] D. Grasso, F. Califano, F. Pegoraro, and F. Porcelli, Ion larmor radius effects in collisionless reconnection, *Plasma Physics Reports* **26**, 512 (2000).
- [47] This initial configuration is approximately an equilibrium but it is unstable to coalescence instability [78]. We choose this configuration instead of the typical Harris sheet [79] for consistency with the study of the inverse magnetic energy transfer problem discussed below. However, we do not expect the results to be sensitive to the specific configuration chosen.
- [48] H. Isobe, H. Takasaki, and K. Shibata, Measurement of

- the energy release rate and the reconnection rate in solar flares, *The Astrophysical Journal* **632**, 1184 (2005).
- [49] S. Zenitani and M. Hesse, The role of the Weibel instability at the reconnection jet front in relativistic pair plasma reconnection, *Physics of Plasmas* **15**, 022101 (2008), <https://doi.org/10.1063/1.2836623>.
- [50] J. F. Drake, M. A. Shay, and M. Swisdak, The Hall fields and fast magnetic reconnection, *Physics of Plasmas* **15**, 042306 (2008), <https://aip.scitation.org/doi/pdf/10.1063/1.2901194>.
- [51] N. Bessho and A. Bhattacharjee, Fast magnetic reconnection and particle acceleration in relativistic low-density electron-positron plasmas without guide field, *The Astrophysical Journal* **750**, 129 (2012).
- [52] L.-J. Chen, M. Hesse, S. Wang, D. Gershman, R. Ergun, J. Burch, N. Bessho, R. Torbert, B. Giles, J. Webster, *et al.*, Electron diffusion region during magnetopause reconnection with an intermediate guide field: Magnetospheric multiscale observations, *Journal of Geophysical Research: Space Physics* **122**, 5235 (2017).
- [53] N. Loureiro, A. Schekochihin, and A. Zocco, Fast collisionless reconnection and electron heating in strongly magnetized plasmas, *Physical Review Letters* **111**, 025002 (2013).
- [54] R. Numata and N. Loureiro, Ion and electron heating during magnetic reconnection in weakly collisional plasmas, *Journal of Plasma Physics* **81**, 305810201 (2015).
- [55] A. Mallet, The onset of electron-only reconnection, *Journal of Plasma Physics* **86**, 905860301 (2020).
- [56] B. Goldstein, E. Smith, A. Balogh, T. Horbury, M. Goldstein, and D. Roberts, Properties of magnetohydrodynamic turbulence in the solar wind as observed by *ulysses* at high heliographic latitudes, *Geophysical Research Letters* **22**, 3393 (1995).
- [57] The fit is slightly worse for $k_{\perp, \max}$ than for \mathcal{E} due to the discrete nature of this diagnostic and the limited change in the value of $k_{\perp, \max}$, given the constrained size of the simulation domain.
- [58] J. Cho and A. Lazarian, Simulations of electron magnetohydrodynamic turbulence, *The Astrophysical Journal* **701**, 236 (2009).
- [59] S. S. Cerri, D. Grošelj, and L. Franci, Kinetic plasma turbulence: recent insights and open questions from 3d3v simulations, *Frontiers in Astronomy and Space Sciences* **6**, 64 (2019).
- [60] Before the system settles into a natural state of decaying turbulence described by our theory, it undergoes a transient stage characterized by the development of strong turbulence. An essential indicator of strong turbulence is the establishment of critical balance, where flux tubes initially confined to box length break in the z -direction. This reduction in the parallel coherence length l is captured by the first two data points in Fig. 2 (b).
- [61] S. Boldyrev and J. C. Perez, Spectrum of kinetic-Alfvén turbulence, *The Astrophysical Journal Letters* **758**, L44 (2012).
- [62] J. Eastwood, T. Phan, P. Cassak, D. Gershman, C. Haggerty, K. Malakit, M. Shay, R. Mistry, M. Øieroset, C. Russell, *et al.*, Ion-scale secondary flux ropes generated by magnetopause reconnection as resolved by *mms*, *Geophysical research letters* **43**, 4716 (2016).
- [63] W. Sun, J. Slavin, A. Tian, S. Bai, G. Poh, M. Akhavan-Tafti, S. Lu, S. Yao, G. Le, R. Nakamura, *et al.*, *Mms* study of the structure of ion-scale flux ropes in the earth's cross-tail current sheet, *Geophysical Research Letters* **46**, 6168 (2019).
- [64] M. Zhou, V. Zhdankin, M. W. Kunz, N. F. Loureiro, and D. A. Uzdensky, Spontaneous magnetization of collisionless plasma, *Proceedings of the National Academy of Sciences* **119**, e2119831119 (2022).
- [65] M. Zhou, V. Zhdankin, M. W. Kunz, N. F. Loureiro, and D. A. Uzdensky, Magnetogenesis in a collisionless plasma: from weibel instability to turbulent dynamo, *The Astrophysical Journal* **960**, 12 (2023).
- [66] E. Priest and T. Forbes, *Magnetic Reconnection: MHD Theory and Applications* (Cambridge University Press, 2000).
- [67] M. Yamada, R. Kulsrud, and H. Ji, Magnetic reconnection, *Reviews of Modern Physics* **82**, 603 (2010).
- [68] M. Hesse and P. Cassak, Magnetic reconnection in the space sciences: Past, present, and future, *Journal of Geophysical Research: Space Physics* **125**, e2018JA025935 (2020).
- [69] R. M. Kulsrud and E. G. Zweibel, On the origin of cosmic magnetic fields, *Reports on Progress in Physics* **71**, 046901 (2008).
- [70] E. S. Weibel, Spontaneously growing transverse waves in a plasma due to an anisotropic velocity distribution, *Physical Review Letters* **2**, 83 (1959).
- [71] T. J. Schep, F. Pegoraro, and B. N. Kuvshinov, Generalized two-fluid theory of nonlinear magnetic structures, *Physics of Plasmas* **1**, 2843 (1994).
- [72] S. Wang, L. M. Kistler, C. G. Mouikis, and S. M. Petriner, Dependence of the dayside magnetopause reconnection rate on local conditions, *Journal of Geophysical Research: Space Physics* **120**, 6386 (2015).
- [73] J. Zheng and Q. Hu, Observational evidence for self-generation of small-scale magnetic flux ropes from intermittent solar wind turbulence, *The Astrophysical Journal Letters* **852**, L23 (2018).
- [74] Y. Chen, Q. Hu, and J. A. le Roux, Analysis of small-scale magnetic flux ropes covering the whole *ulysses* mission, *The Astrophysical Journal* **881**, 58 (2019).
- [75] Y. Chen and Q. Hu, Small-scale magnetic flux ropes and their properties based on in situ measurements from the *parker* solar probe, *The Astrophysical Journal* **924**, 43 (2022).
- [76] J. Drake, O. Agapitov, M. Swisdak, S. Badman, S. Bale, T. Horbury, J. C. Kasper, R. MacDowall, F. Mozer, T. Phan, *et al.*, Switchbacks as signatures of magnetic flux ropes generated by interchange reconnection in the corona, *Astronomy & Astrophysics* **650**, A2 (2021).
- [77] M. Zhou, Z. Liu, and N. F. Loureiro, Electron heating in kinetic-Alfvén-wave turbulence, *Proceedings of the National Academy of Sciences* **120**, e2220927120 (2023).
- [78] J. M. Finn and P. K. Kaw, Coalescence instability of magnetic islands, *The Physics of Fluids* **20**, 72 (1977).
- [79] E. G. Harris, On a plasma sheath separating regions of oppositely directed magnetic field, *Il Nuovo Cimento* (1955-1965) **23**, 115 (1962).
- [80] P. Sweet, 14. the neutral point theory of solar flares, in *Symposium-International Astronomical Union*, Vol. 6 (Cambridge University Press, 1958) pp. 123–134.
- [81] E. N. Parker, Sweet's mechanism for merging magnetic fields in conducting fluids, *Journal of Geophysical Research* **62**, 509 (1957).
- [82] D. Grošelj, S. S. Cerri, A. B. Navarro, C. Willmott, D. Told, N. F. Loureiro, F. Califano, and F. Jenko, Fully

- kinetic versus reduced-kinetic modeling of collisionless plasma turbulence, *The Astrophysical Journal* **847**, 28 (2017).
- [83] V. Fadeev, I. Kvabtskhava, and N. Komarov, Self-focusing of local plasma currents, *Nuclear fusion* **5**, 202 (1965).
- [84] R. A. Fonseca, L. O. Silva, F. S. Tsung, V. K. Decyk, W. Lu, C. Ren, W. B. Mori, S. Deng, S. Lee, T. Katsouleas, *et al.*, Osiris: A three-dimensional, fully relativistic particle in cell code for modeling plasma based accelerators, in *Computational Science—ICCS 2002: International Conference Amsterdam, The Netherlands, April 21–24, 2002 Proceedings, Part III 2* (Springer, 2002) pp. 342–351.

Supplemental Material

Zhuo Liu¹, Caio Silva¹, Lucio M. Milanese², Muni Zhou³, Noah R. Mandell⁴, and
Nuno F. Loureiro¹

¹Plasma Science and Fusion Center, Massachusetts Institute of Technology,
Cambridge, MA 02139, USA

²Proxima Fusion GmbH, Munich, Germany

³School of Natural Sciences, Institute for Advanced Study, Princeton, NJ 08544, USA

⁴Princeton Plasma Physics Laboratory, Princeton, NJ 08543, USA

1 Magnetic reconnection simulations: further numerical details and characterization

In the electron-only reconnection model discussed, we made two assumptions regarding the current sheets. First, that their width is comparable to the electron skin depth, $\delta_x \sim d_e$. Second, that their length is independent of kinetic parameters, i.e., $\delta_y \sim R$, where R is the island size. Table 1 summarizes the parameters of all the simulations appearing in Fig. 1 in the main paper. We validate these assumptions with the three simulations from the column of $\rho_i/R = 1.82$ ($\rho_i = 1.0$).

The time evolution of the reconnection rate (in normalization of Alfvénic time in the perpendicular plane), defined as the time derivative of the magnetic flux between the X- and the O-points, from the simulation with $d_e = 0.1$ is shown in Fig. 1(a). A contour plot of the out-of-plane current density J_z , at the time of maximum reconnection rate (identified by the blue star in Fig. 1(a)), is shown in Fig. 1(b) and Fig. 1(c): (b) shows the entire simulation domain, whereas in (c) we zoom in on the current sheet. Interestingly, we observe no disruption or plasmoid instability as the current sheet shrinks down to the d_e scale, which seems to be at odds with previous analytical analysis [1]. We also note that our reconnection rate formula is not a steady-state solution ($\partial/\partial t \neq 0$), different from the derivation in [1].

In Fig. 2, we plot the out-of-plane current along the two symmetry axes, $y = 0$ and $x = 0$ (illustrated by the dashed lines in Fig. 1(b)) for simulations with different values of d_e . Fig. 2(a) shows that the

Table 1: Summary of the key parameters of the reconnection simulations in Fig. 1 of the main paper. In the ‘‘Regime’’ row, ‘‘I’’ refers to ion-coupled, and ‘‘E’’ refers to electron-only. The ‘‘ N ’’ row refers to the number of grid points in one either direction, so that the grid size in each direction, Δ , is $2\pi/N$. $R \approx 0.55$ for all simulations.

ρ_i/R	0.023	0.045	0.091	0.18	0.36	0.91	1.82	3.64
Regime	I	I	I	I	I	E	E	E
d_e	0.0025	0.0025	0.005	0.01	0.02	0.05, 0.1, 0.2	0.05, 0.1, 0.2	0.1, 0.2
N	8192	8192	8192	4096	2048	4096, 2048, 1024	4096, 2048, 1024	2048, 1024
d_e/Δ	3.3	3.3	6.5	6.5	6.5	32.6	32.6	32.6

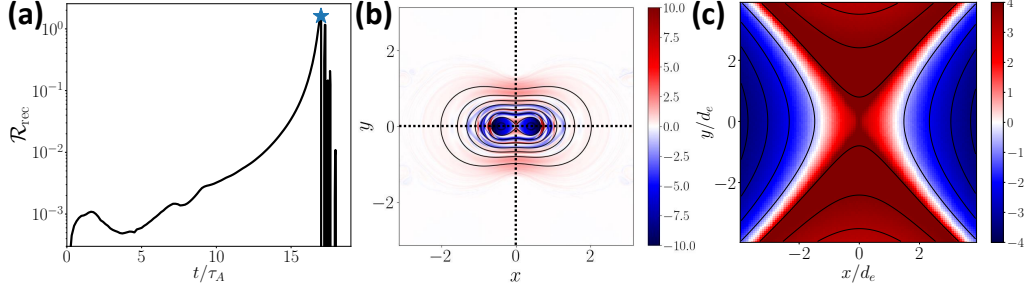


Figure 1: (a) Time trace of the reconnection rate, \mathcal{R}_{rec} of the reconnection simulation with $\rho_i/R = 1.82$ ($\rho_i = 1.0$) and $d_e = 0.1$. (b) Snapshot of out-of-plane current density (color) and parallel magnetic flux at the time of the maximum reconnection rate (the blue star in (a)). (c) Zoom-in of the reconnecting current sheet in (b).

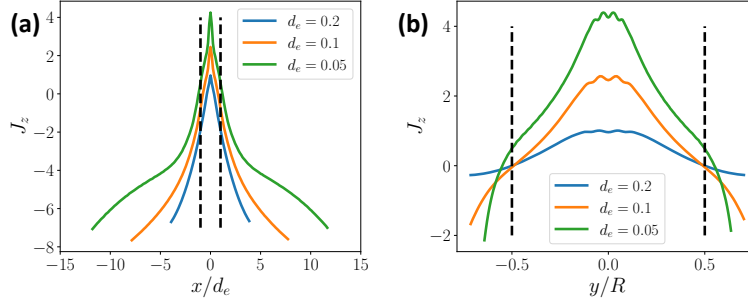


Figure 2: Out-of-plane current density (J_z) along the horizontal dashed line (a) and vertical dashed line (b) in Fig. 1 (a) for simulations with $\rho_i/R = 1.82$ ($\rho_i = 1.0$) but different values of d_e . In (a), each curve is normalized to its own d_e on the horizontal axis. The vertical dashed lines indicate $\pm d_e$. In (b), R is the initial island size. The vertical dashed lines indicate $\pm 0.5R$.

width of the current sheet is always approximately $2d_e$ regardless of the value of d_e , which confirms that $\delta_x \sim d_e$ is indeed reached. In Fig. 2(b), all reconnecting current sheet lengths are close to R , validating that $\delta_y \sim 0.5R$. Another interesting observation from Fig. 2(b) is the small depression in J_z around the X-point. While we do not have a direct explanation for this feature, we think it is associated with the innermost structure that forms below d_e scale in the x direction (if one zooms in Fig. 2(a)). The development of this sub- d_e feature in the x direction is a known numerical phenomenon caused by the hyper-resistive term that becomes significant at the grid scale. However, it has been pointed out that this very localized current spike carries negligible current and thus does not affect the reconnection process itself [2, 3].

All the simulations shown above and in the main paper have $\rho_i/d_e \leq 20$ in order not to interfere with the low-beta ordering that underlies the KREHM equations (see [4]) that we use. However, we also performed simulations which, while in formal violation of that ordering, further demonstrate the correctness of our reconnection rate derivation — see Fig. 3.

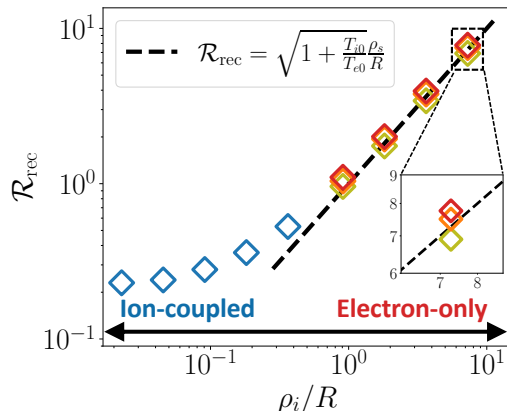


Figure 3: Dimensionless peak reconnection rates, \mathcal{R}_{rec} , from simulations with different values of ρ_i/R . In the electron-only regime ($\rho_i \gtrsim R > d_e$), red, orange, and yellow symbols refer to simulations with $d_e/R = 0.09, 0.18, 0.36$, respectively. In the ion-coupled regime ($R > \rho_i > d_e$), we set $d_e/\rho_i = 0.1$ (except for the leftmost data-point, where $d_e/\rho_i = 0.2$).

2 Electron-only reconnection rate at plasma beta of order unity

In the main paper, we derive an electron-only strong-guide-field reconnection model using a two-field isothermal fluid description valid at low plasma beta. Here we propose a generalization of that model to the case $\beta_e \sim 1$.

Under the same approximation of strong guide field as invoked in the main paper, it is possible to obtain a fluid model valid for $\beta_e \sim 1$ at scales $\rho_i^{-1} \ll k_\perp \ll \rho_e^{-1}$: the so-called electron-reduced MHD (ERMHD) [5]. In two dimensions (i.e., in the plane perpendicular to the guide field) the equations are:

$$\frac{\partial}{\partial t} \left[\left(2 + \beta_i \left(1 + \frac{Z}{\tau} \right) \right) \frac{\delta n_e}{n_{0e}} \right] = \frac{2ed_e^2}{cm_e B_z} \{ A_z, \nabla_\perp^2 A_z \}, \quad (1)$$

$$\frac{\partial A_z}{\partial t} = -\frac{cT_{0i}}{ZeB_z} \left(1 + \frac{Z}{\tau} \right) \left\{ A_z, \frac{\delta n_e}{n_{0e}} \right\}, \quad (2)$$

where $\beta_i = 4\pi n_{0i} m_i / B_z^2$ is the ion beta, $\tau = T_{i0}/T_{e0}$ is the temperature ratio, and Z is the ion charge (assumed to be one in the main paper).

The first thing to note is that this model cannot rigorously be used to study reconnection because the frozen-flux breaking mechanisms (electron inertia and finite electron Larmor radius effects) are ordered out. However, from the low-beta derivation presented in the main paper, we concluded that the flux-breaking term (electron inertia (d_e) in our model) does not affect the term balancing, and the resulting reconnection rate does not depend on it. This leads us to hypothesize that a similar derivation can be applied to the ERMHD equations above; that is, even if this model could be consistently extended to include both electron inertia and electron finite Larmor radius, the presence of those terms would not affect term balancing and, thus, the reconnection rate can be obtained from the equations such as they are. Therefore, following a procedure entirely similar to that of the main paper, we obtain

$\tau_{\text{rec}} = \mathcal{R}_{\text{rec}}^{-1} R / v_{A,\perp}$, where

$$\mathcal{R}_{\text{rec}} \sim \sqrt{\frac{\beta_i(1 + Z/\tau)}{2 + \beta_i(1 + Z/\tau)}} \frac{d_i}{R}. \quad (3)$$

While this expression needs thorough numerical validation, we find that it agrees remarkably well with the reconnection rates in the electron-only regime reported in [6] (the two leftmost data points in Fig. 4 (b) in that paper) using the parameters given in the paper and assuming R to be half of the domain size.

3 Inverse magnetic energy transfer simulations: further details

In the 2D magnetic energy transfer simulations described in the main paper, we initialized a spectrum of random fields at small sub-ion scales. As the simulation evolves, the magnetic structures progressively grow in size (via their coalescence), as evidenced by the visualizations in Fig. 4.

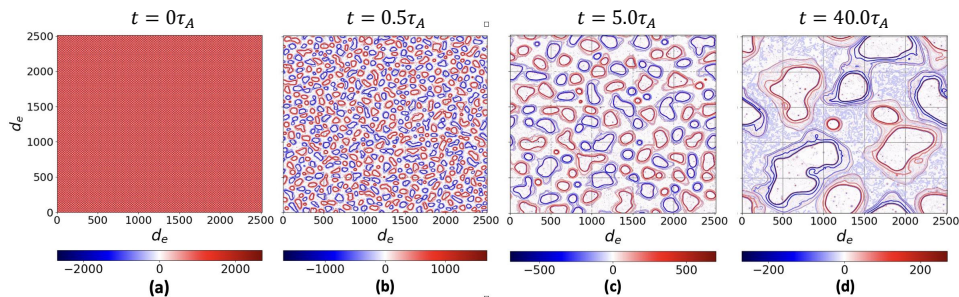


Figure 4: Out-of-plane current density for the island merger simulation (2D) at progressively later times.

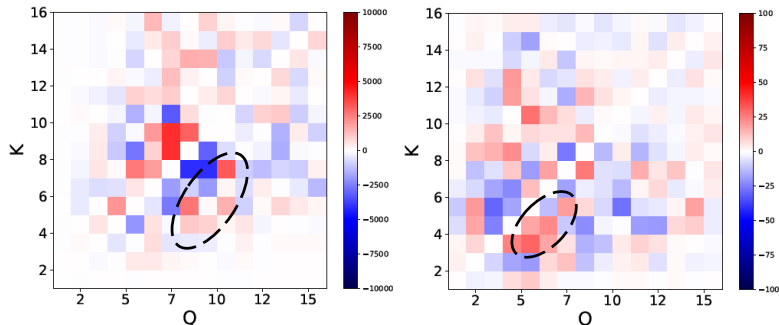


Figure 5: Averaged magnetic energy transfer from shell Q to shell K , $T_{bb}(Q, K)$, at $t \approx 0.35\tau_A$ (left) and $t \approx 4.5\tau_A$ (right) for the 3D island merger simulation. The circled region identifies wavenumbers for which there is strong inverse energy transfer.

A more quantitative determination of inverse (and direct) energy transfer is obtained via shell-to-shell energy transfer functions. In the limit of $1/\rho_i < k_\perp < 1/d_e$ the equation for the (z component of

the) vector potential reduces to

$$\frac{\partial A_z}{\partial t} = -\frac{c(T_{0e} + T_{0i})}{e} \frac{1}{B_0} \left\{ A_z, -\frac{e}{T_{0i}} \varphi \right\} + \frac{\partial}{\partial z} \left(-\frac{e}{T_{0i}} \varphi \right). \quad (4)$$

This equation is formally analogous to the vector potential equation in the RMHD framework [7]. Therefore, we can define the shell-filtered variables, similar to the RMHD case, as

$$\begin{aligned} \mathbf{B}_\perp^K(\mathbf{x}_\perp, z) &= \sum_{K < k_\perp \leq K+1} \mathbf{B}_\perp(\mathbf{k}_\perp, z) e^{i\mathbf{k}_\perp \cdot \mathbf{x}_\perp}, \\ \mathbf{u}_\perp^K(\mathbf{x}_\perp, z) &= \sum_{K < k_\perp \leq K+1} \mathbf{u}_\perp(\mathbf{k}_\perp, z) e^{i\mathbf{k}_\perp \cdot \mathbf{x}_\perp}, \end{aligned} \quad (5)$$

where $\mathbf{u}_\perp = \hat{z} \times \nabla(c\varphi/B_0)$ is the perpendicular drift velocity and φ is related to the electron density fluctuations as $\delta n_e/n_{0e} \approx -e\varphi/T_{0e}$ via Poisson's law. Then, the transfer of magnetic energy from shell Q to shell K is

$$T_{bb}(Q, K) \propto - \left\langle \int d^2\mathbf{x}_\perp \mathbf{B}_\perp^K \cdot (\mathbf{u}_\perp \cdot \nabla_\perp) \mathbf{B}_\perp^Q \right\rangle_z. \quad (6)$$

In Figure 5, we show the energy transfer diagrams for the 3D simulation at two different times. The red color below the diagonal in these plots denotes positive energy transfer from high k_\perp to low k_\perp and thus indicates an inverse energy transfer. The red color above the diagonal in these plots denotes positive energy transfer from low k_\perp to high k_\perp and thus indicates a direct energy transfer; and vice-versa for the blue color.

It can be seen that there are both strong direct and inverse cascades in the simulation. In the left panel ($t \approx 0.35\tau_A$), the circled area identifies wavenumbers where strong inverse cascade occurs (mostly from shells $Q = 10, 8$ to $K = 7, 5$). As expected, the inverse cascade is not local. Each generation of island merger will cause k_\perp to be divided by $\sqrt{2}$, which is consistent with the fact that the inverse energy transfer from shell 10 to 7 is the strongest. Note that this is also consistent with the fact that the peak of the magnetic spectrum at this time is located at around $k_\perp = 7$ (see Fig. 2(a) in the main paper, $k_{\perp, \max} \approx 7$ at $t \approx 0.35\tau_A$). In the right panel ($t \approx 4.5\tau_A$), the magnetic energy is more concentrated around $k_\perp = 4, 5$, which aligns with the fact that the most intense inverse energy transfer happens around this region.

Finally, we note that these results are very different from the RMHD case, where the direct cascade is much stronger [7]. As discussed in the main paper, we believe this is because magnetic mergers happen on a time scale comparable to the nonlinear eddy turnover rate in the sub-ion scales. Therefore, the inverse cascade can happen as fast as the forward cascade, leading to a strong inverse cascade, comparable to the direct cascade.

4 Inverse energy transfer in the non-isothermal case

4.1 Equations

In the main paper, we adopt a two-field isothermal gyrofluid model, which is equivalent to the isothermal version of the kinetic reduced electron heating model (KREHM) [4]. To validate that the isothermal limit does not affect the main conclusions of the paper, we solve the full KREHM equations and compare the results with the isothermal counterpart.

The KREHM model is a rigorous asymptotic reduction of (δ - f) gyrokinetics valid for plasma at low electron plasma-beta. The perturbed electron distribution function, to lowest order in $\sqrt{m_e/m_i}$,

is expanded as $\delta f_e = g_e + (\delta n_e/n_{0e} + 2v_z u_{ze}/v_{\text{the}}^2)F_{0e}$, where F_{0e} is the equilibrium Maxwellian defined with the mean electron temperature T_{0e} and $v_{\text{the}} = \sqrt{2T_{0e}/m_e}$ is the corresponding thermal speed, and δn_e and u_{ze} are the zeroth and first moments of the perturbed electron distribution: the perturbed electron density and the bulk electron velocity in the guide-field direction, respectively. The latter can be related to the parallel vector potential, A_z , via the parallel component of Ampère's law which, under the mass ratio expansion adopted by KREHM, reduces to $u_{ze} = (e/cm_e)d_e^2\nabla_{\perp}^2 A_z$, where $d_e = c/\omega_{pe}$ is the electron skin depth. All moments of δf_e higher than δn_e and u_{ze} are contained in the (reduced) distribution function g_e . The equations are:

$$\frac{1}{n_0} \frac{d\delta n_e}{dt} = \hat{\mathbf{b}} \cdot \nabla \frac{e}{cm_e} d_e^2 \nabla_{\perp}^2 A_z, \quad (7)$$

$$\frac{d}{dt} (A_z - d_e^2 \nabla_{\perp}^2 A_z) = -c \frac{\partial \varphi}{\partial z} + \hat{\mathbf{b}} \cdot \nabla \left(\frac{\delta n_e}{n_{0e}} + \frac{\delta T_{\parallel e}}{T_{0e}} \right), \quad (8)$$

$$\frac{dg_e}{dt} - \frac{v_{\parallel}}{B_z} \left\{ A_z, g_e - \frac{\delta T_{\parallel e}}{T_{0e}} F_{0e} \right\} = C[g_e] + \left(1 - \frac{2v_{\parallel}^2}{v_{\text{the}}^2} \right) F_{0e} \hat{\mathbf{b}} \cdot \nabla \frac{e}{cm_e} d_e^2 \nabla_{\perp}^2 A_z, \quad (9)$$

$$\frac{\delta n_e}{n_{0e}} = \frac{T_{0e}}{T_{0i}} (\hat{\Gamma}_0 - 1) \frac{e\varphi}{T_{0e}}, \quad (10)$$

where $C[g_e]$ is the collision operator and $\delta T_{\parallel e}$ is the perturbed electron temperature in the parallel direction, i.e., $\delta T_{\parallel e}/T_{0e} = (1/n_{0e}) \int d^3\mathbf{v} (2v_{\parallel}^2/v_{\text{the}}^2) g_e$.

As pointed out in Ref. [4], Eq. (9) does not contain any dependence on v_{\perp} as long as the collision operator does not introduce one. So far as that is the case, we can expand $g_e = g_e(\mathbf{r}, v_z, t)$ in terms of Hermite polynomials as $g_e(\mathbf{r}, v_z, t) = 1/\sqrt{2^m m!} \sum_{m=2}^{\infty} H_m(v_z/v_{\text{the}}) g_m(\mathbf{r}, t) F_{0e}(v_z)$ (with $g_0 = g_1 = 0$ because δn_e and u_{ze} have been explicitly separated in the decomposition of δf_e adopted above). Eq. (9) can then be decomposed into a series of coupled fluid-like equations for the Hermite coefficients g_m (for $m \geq 2$):

$$\frac{dg_m}{dt} = v_{\text{the}} \hat{\mathbf{b}} \cdot \nabla \left(\sqrt{\frac{m+1}{2}} g_{m+1} + \sqrt{\frac{m}{2}} g_{m-1} - \delta_{m,1} g_2 \right) + \sqrt{2} \delta_{m,2} \hat{\mathbf{b}} \cdot \nabla \frac{e}{cm_e} d_e^2 \nabla_{\perp}^2 A_z - C[g_m]. \quad (11)$$

The isothermal approximation that we work with in the main paper corresponds to setting $g_e = 0$, in which case Eq. (9) (or, equivalently, Eq. (11)) is not necessary. However, note that $g_e = 0$ is only an admissible solution of Eq. (9) if the last term on the RHS also vanishes — a situation that cannot describe reconnecting and/or turbulent systems. As such, the isothermal limit is not justified: formally, one needs to retain finite g_e , which enables electron Landau damping (via a cascade of energy to high-order Hermite moments where small collisions can act efficiently); and, indeed, this dissipation channel has been shown in related studies to be dominant [4, 8, 9]. However, given that electron heating is not the object of this study, and noting that the isothermal approximation makes for a much more computationally efficient model, we believe this is an acceptable approximation; and check in the next section that doing away with the isothermal approximation does not change the main results of our paper.

4.2 Simulations

We conduct a two-dimensional non-isothermal simulation and compare it with its isothermal counterpart. The initial condition is an array of single-size magnetic islands, i.e., $A_z(x, y) = A_0 \cos(k_0 x) \cos(k_0 y)$, with $k_0 = 10$. The simulations are performed in a doubly periodic box of dimensions $L_x \times L_y$, where $L_x = L_y = 2\pi$, and the spatial grid size is 1024×1024 . For the electron velocity space, we retain 96

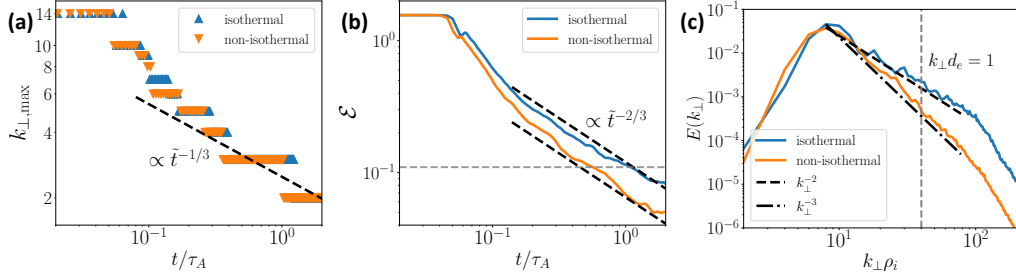


Figure 6: Comparison between the isothermal and the non-isothermal simulations. (a) Evolution of the wavenumber corresponding to the peak of the magnetic energy spectrum; (b) Evolution of domain-averaged magnetic energy; and (c) Magnetic spectra at $t = 0.3\tau_A$.

Hermite polynomials, i.e., $M = 96$. We set $\rho_i = 2.0$ and $d_e = 0.04$ ¹, ensuring that most of the islands' evolution remains within the sub- ρ_i regime. A hyper-collision term of the form $\nu_{\text{coll}}m^6$ is added to the R.H.S. of Eq. (11) for $m > 2$, with ν_{coll} set to remove energy at the smallest velocity scale (determined by M , the order of the highest Hermite polynomial kept in simulations).

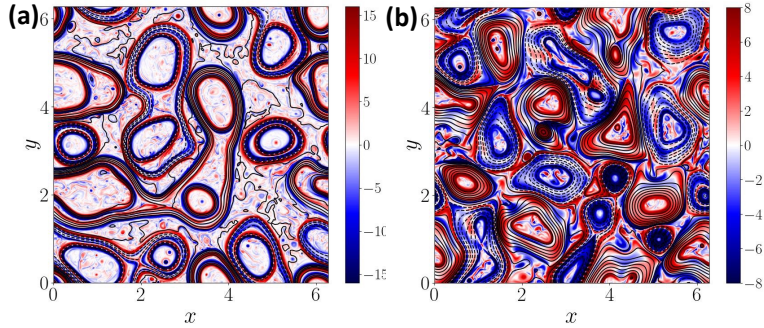


Figure 7: Out-of-plane current density (colors) and parallel magnetic flux (contours) for (a) isothermal simulation and (b) non-isothermal simulation when the system dissipates 88% of its initial magnetic energy (corresponding to the horizontal gray line in Fig. 6 (b)).

We plot the temporal evolution of the wavenumber corresponding to the peak of the magnetic spectrum ($k_{\perp, \max}$) and total magnetic energy (\mathcal{E}) in Figs. 6(a) and 6(b), respectively. The magnetic energy spectra at $t = 0.3\tau_A$ from the two simulations are shown in Fig. 6(c). Comparing the non-isothermal and isothermal cases, we observe mostly overlapping $k_{\perp, \max}$ data points but somewhat faster magnetic energy dissipation in the former, as expected, due to the availability of the Landau damping energy dissipation channel (which is activated primarily in the vicinity of current sheets [9]). Nevertheless, both time traces exhibit reasonable agreement with the respective power laws (because allowing for Landau damping does not interfere with either the travel time or the reconnection time).

More notable differences emerge in the magnetic spectra: while the isothermal simulation aligns well with the scaling k_{\perp}^{-2} , indicative of highly localized and sharp current sheets (a Burgers' spectrum) [10], the non-isothermal case displays a significantly steeper scaling close to k_{\perp}^{-3} . In Fig. 7 we show the

¹The parameters selected here may formally violate the KREHM low-beta ordering. However, the primary objective of this section is to compare the full KREHM simulations with their isothermal counterparts. These parameters are intentionally chosen to maximize scale separation, enabling a clear isolation and analysis of the dominant physical processes involved.

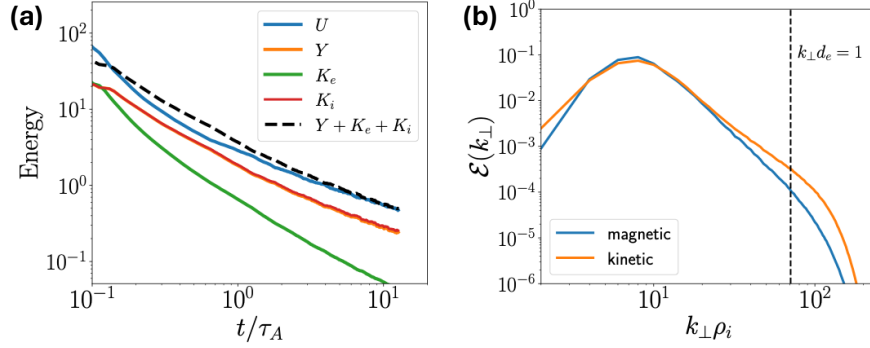


Figure 8: (a) Time trace of the different components of free energy from the 3D simulation presented in the main paper. (b) Magnetic and kinetic energy spectra at $t \approx 4.9\tau_A$.

contour plots of J_z and A_z of the two simulations when the system dissipates 88% of its initial magnetic energy (corresponding to the horizontal gray line in Fig. 6(a)). A visual inspection reveals remarkably smoother current sheets between the magnetic islands in the non-isothermal run, likely accounting for the steeper spectrum observed in Fig. 6(c). Our explanation posits that Landau damping and the associated electron heating occur predominantly at the places where the current gradient is large. This argument can be readily inferred from Eq. (9), where the source term for g_e is proportional to the gradient of the current (refer to [9] for more details). Consequently, in the non-isothermal simulation, most Landau damping happens around sharp current sheets, effectively dissipating magnetic energy and mitigating sharpness in these current structures.

We note that the isothermal run here exhibits a different power law in the magnetic spectrum compared with the 3D simulation we presented in the main paper (k_\perp^{-2} rather than $k_\perp^{-8/3}$). We think this is because the 2D system is less turbulent than its 3D counterpart, and the direct turbulent cascade is too weak. Therefore, the magnetic spectrum here is mostly determined by the current sheet structures rather than Alfvén wave packets. In the non-isothermal 3D scenario, we anticipate a steepening of the $k_\perp^{-8/3}$ power law due to Landau damping [9].

5 Equipartition between magnetic and kinetic energy

In the isothermal limit ($g_e = 0$), Eqs. (7,8) conserve a quadratic invariant, referred to as the (fluid) free energy,

$$\begin{aligned}
 W &\equiv U + K_i + K_e + Y \\
 &\equiv \int \frac{d^3\mathbf{r}}{V} \left[\frac{|\nabla_\perp A_z|^2}{8\pi} + (1 - \hat{\Gamma}_0) \frac{e^2 n_{0e} \varphi^2}{2T_{0i}} + \frac{d_e^2 |\nabla_\perp^2 A_z|^2}{8\pi} + \left(\frac{\delta n_e}{n_{0e}} \right)^2 n_{0e} T_{0e} \right], \quad (12)
 \end{aligned}$$

where U , K_i , K_e , and Y correspond to the magnetic energy, the ion perturbed entropy, the kinetic energy of the parallel electron flow, and the electron density variance, respectively [4].

In the main paper, we assumed electron density and magnetic energy fluctuations are comparable, i.e., $U \sim Y$, for deriving the in-plane advection velocity u_\perp . To validate this assumption, we plot in Fig. 8 the time traces and spectra of the components of the energy invariant from the 3D simulation we presented in the main paper. From the time trace plot, the key observations are: first, there is

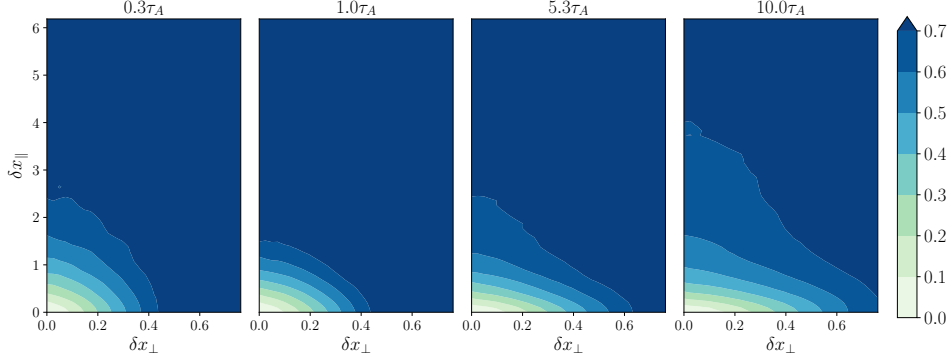


Figure 9: Contour plots of the normalized structure function $SF_2(\delta x_\perp, \delta x_\parallel)/SF_2(\delta x_\perp, \delta x_\parallel)_{\max}$ for the three-dimensional run at different times.

approximate equipartition between magnetic energy and the remaining terms, i.e., $K_e + K_i + Y \approx U$, especially after $t \approx 1.0\tau_A$ (corresponding to the time the strong turbulence established in the system as discussed in the main paper); second, K_e is much smaller than the other terms; third, $K_i \approx Y$, which is expected because Eq. (10) reduces to $\delta n_e/n_{0e} \sim -e\varphi/T_{0i}$ when $k_\perp \rho_i \gg 1$. Therefore, $Y = 0.5(Y+Y) \approx 0.5(Y+K_i) \approx 0.5(Y+K_i+K_e) \approx 0.5U$, and thus $U \sim Y$ is a valid assumption throughout the simulation. The spectra plot confirms that the scale-by-scale equipartition is reasonable, especially at the energy-containing scales. The equipartition confirmed by our simulation is in fact implied by our theory. From Eqs. (A5) and (A7), we find $\delta n_e/n_{0e} \sim B_\perp$. In other words, the reconnection process itself is characterized by energy equipartition.

6 Five-point second-order structure function

To obtain statistical information on the growth of flux tubes, and to test the assumption of critical balance, we calculate the five-point second-order structure function of the magnetic field,

$$SF_2(\delta \mathbf{x}) = \frac{1}{\sqrt{35}} \langle |\mathbf{B}(\mathbf{x} + 2\delta \mathbf{x}) - 4\mathbf{B}(\mathbf{x} + \delta \mathbf{x}) + 6\mathbf{B}(\mathbf{x}) - 4\mathbf{B}(\mathbf{x} - \delta \mathbf{x}) + \mathbf{B}(\mathbf{x} - 2\delta \mathbf{x})|^2 \rangle_x, \quad (13)$$

where the angle brackets denote the average over \mathbf{x} . The local magnetic field can be defined as $\mathbf{B}_{\text{loc}} = [\mathbf{B}(\mathbf{x} - 2\delta \mathbf{x}) + \mathbf{B}(\mathbf{x} - \delta \mathbf{x}) + \mathbf{B}(\mathbf{x}) + \mathbf{B}(\mathbf{x} + \delta \mathbf{x}) + \mathbf{B}(\mathbf{x} + 2\delta \mathbf{x})]/16$. We can then define the local unit vector parallel to the local magnetic field as $\hat{\mathbf{b}}_m = \mathbf{B}_{\text{loc}}/|\mathbf{B}_{\text{loc}}|$. The local coordinate system can thus be defined as $\delta x_\perp \equiv |\hat{\mathbf{b}}_m \times \delta \mathbf{x}|$, $\delta x_\parallel \equiv |\hat{\mathbf{b}}_m \cdot \delta \mathbf{x}|$. We emphasize that the parallel and perpendicular directions here are defined with respect to the local magnetic field (as they should in order to assess the validity of the critical balance approximation) rather than the guide field, which is different from the definition of “parallel” and “perpendicular” in the main paper. The relation of the correlation lengths between the parallel and the perpendicular directions thus can be determined from the contours of $SF_2(\delta \mathbf{x}) = SF_2(\delta x_\perp, \delta x_\parallel)$.

Fig. 9 shows plots of $SF_2(\delta x_\perp, \delta x_\parallel)$ normalized to its maximum value at different times from the 3D simulation we discussed in the main paper. The parallel correlation length l (characteristic length of flux tubes) and perpendicular correlation length R (characteristic radius of flux tubes) can be defined as the intersection of some contour line $SF_2(\delta x_\perp, \delta x_\parallel)/SF_2(\delta x_\perp, \delta x_\parallel)_{\max} = C$ with δx_\perp axis and δx_\parallel

axis, respectively. Empirically, we choose $C = 0.68$, corresponding to the largest value at which the contour lines are not severely affected by noise.

References

- [1] Alfred Mallet. The onset of electron-only reconnection. *Journal of Plasma Physics*, 86(3):905860301, 2020.
- [2] B. Rogers and L. Zakharov. Collisionless $m=1$ reconnection in tokamaks. *Physics of Plasmas*, 3(6):2411–2422, 1996.
- [3] D. Grasso, F. Califano, F. Pegoraro, and F. Porcelli. Ion larmor radius effects in collisionless reconnection. *Plasma Physics Reports*, 26:512–518, 2000.
- [4] A. Zocco and A. A. Schekochihin. Reduced fluid-kinetic equations for low-frequency dynamics, magnetic reconnection, and electron heating in low-beta plasmas. *Physics of Plasmas*, 18(10), 2011.
- [5] A. A. Schekochihin, S. C. Cowley, W. Dorland, G. W. Hammett, G. G. Howes, E. Quataert, and T. Tatsuno. Astrophysical gyrokinetics: kinetic and fluid turbulent cascades in magnetized weakly collisional plasmas. *The Astrophysical Journal Supplement Series*, 182(1):310, 2009.
- [6] P. Sharma Pyakure, M. A. Shay, T. D. Phan, J. F. Matthaeus, W. H. and Drake, J. M. TenBarge, C. C. Haggerty, K. G. Klein, P. A. Cassak, T. N. Parashar, et al. Transition from ion-coupled to electron-only reconnection: Basic physics and implications for plasma turbulence. *Physics of Plasmas*, 26(8), 2019.
- [7] Muni Zhou, Nuno F Loureiro, and Dmitri A Uzdensky. Multi-scale dynamics of magnetic flux tubes and inverse magnetic energy transfer. *Journal of Plasma Physics*, 86(4):535860401, 2020.
- [8] N. F. Loureiro, A. A. Schekochihin, and A. Zocco. Fast collisionless reconnection and electron heating in strongly magnetized plasmas. *Physical Review Letters*, 111(2):025002, 2013.
- [9] M. Zhou, Z. Liu, and N. F. Loureiro. Electron heating in kinetic-Alfvén-wave turbulence. *Proceedings of the National Academy of Sciences*, 120(23):e2220927120, 2023.
- [10] J. M. Burgers. A mathematical model illustrating the theory of turbulence. *Advances in Applied Mechanics*, 1:171–199, 1948.